Supplementary information

Untangling cation and anion contributions to refractive index changes in electrical double-layer capacitors

Karen Regules-Medel, Finlay Nelson*, William Hardiman*, Rafael Fuentes Dominguez, Michael Somekh, Sidahmed Abayzeed**

Optics and photonics research group, University of Nottingham, Nottingham, UK

* Authors contributed equally

**Corresponding author – sidahmed.abayzeed2@nottingham.ac.uk

S1 Effect of cation and anion concentrations on electrolyte refractive index

Lorenz-Lorentz equation provides the refractive index of an ionic solution:

$$\frac{n^2-1}{n^2+2} = \sum_j c_j R_j \quad \text{(S1.1)},$$

where n is the refractive index of the solution and c_j is the concentration of the component j in the solution (i.e. ions and solvent) and R_j its corresponding molar refractivity. For the rest of the section, c_j represents the ion concentration in the solution, since the concentration of solvent is assumed to remain fixed.

To understand how the refractive index of the solution changes with the variation in ion concentration, we evaluate the partial derivative $\partial n/\partial c_j$ for each ion.

Let us define a term (g) as the concentration-weighted sum of molar refractivity

$$g = \sum_j c_j R_j \quad \text{(S1.2)}$$

Rearranging Eq. (S1.1) in terms of g, we obtain

$$n^2 = \frac{1+2g}{1-g} \quad \text{(S1.3)}$$

Taking the partial derivative of Eq. (S1.3) gives

$$\frac{\partial n}{\partial c_j} = \frac{\partial n}{\partial g}\frac{\partial g}{\partial c_j}$$

$$\frac{\partial n}{\partial c_j} = \frac{3}{2n\,(1-g)^2}\,R_j \quad \text{(S1.4)}$$

It is important to note the term $(1-g)^2$ cannot be ignored for the case of using 0.1 M NaCl.

Now, we define

$$\frac{\partial n}{\partial c_j} = \beta\,R_j \quad \text{(S1.5)}$$

From Eq. (S1.1) and Eq. (S1.2), we recall that

$$g = \frac{n^2-1}{n^2+2} \quad \text{(S1.6)}$$

Substituting Eq. (S1.6) into Eq. (S1.4) gives

$$\beta = \frac{3}{2n\,(1-g)^2} = \frac{\left(n^2+2\right)^2}{6n} \quad \text{(S1.7)}$$

Assuming $n = 1.33$ for 0.1 M NaCl we obtain $\beta = 1.78$

S2 Electrochemical model validation

We compared the predictions made by our one-dimensional finite element model to the mean-field solutions of the Gouy–Chapman–Stern (GCS) model for the electrical double layer capacitor (EDLC). The Stern potential ϕ_s, defined as the electrostatic potential at the outer Helmholtz plane, was obtained by assuming a constant electric field (i.e., potential gradient) within the Stern layer. Continuity of the electric field across the interface then requires [1]:

$$\phi_s + x_s\frac{d\phi}{dx} - V = 0\text{ , (S2.1)}$$

here, x_s=0.5 nm is the thickness of the Stern layer, $\frac{d\phi}{dx}\big|_{x=x_s}$ is the electrostatic field at the outer Helmholtz plane, and V is the applied voltage. Eq. (S2.1) was solved numerically using the *fzero* function in MATLAB, a root-finding method based on a combination of bisection, secant, and inverse quadratic interpolation techniques.

The total charge density in C/m^2, σ, is then related to the Stern potential using the Grahame Eq. (S2.2):

$$\sigma = \sqrt{8\,k_B T\,\epsilon_0\epsilon c_0}\,\sinh(ze\phi_s\,/\,2k_B T) \text{ (S2.2)}$$

where ϕ_s is the Stern potential, $k_B T$ is the thermal energy term, c_0 is the bulk electrolyte concentration, ϵ_0 and ϵ are the vacuum permittivity and relative permittivity of the electrolyte solution, respectively, z is the valence number, and e is the fundamental charge. We used this form of the Grahame equation for a 1:1 monovalent electrolyte following the approach of Israelachvili [2].

Fig. S2.1a shows the charge density calculated using Eq. (S2.2), alongside the result from the COMSOL finite element model, which was obtained by integrating the excess ionic concentrations multiplied by their respective charges. As shown in Fig. S2.1b, the maximum deviation between the two approaches across the voltage range tested was 0.24%, confirming the accuracy and validity of our COMSOL-based modelling framework.

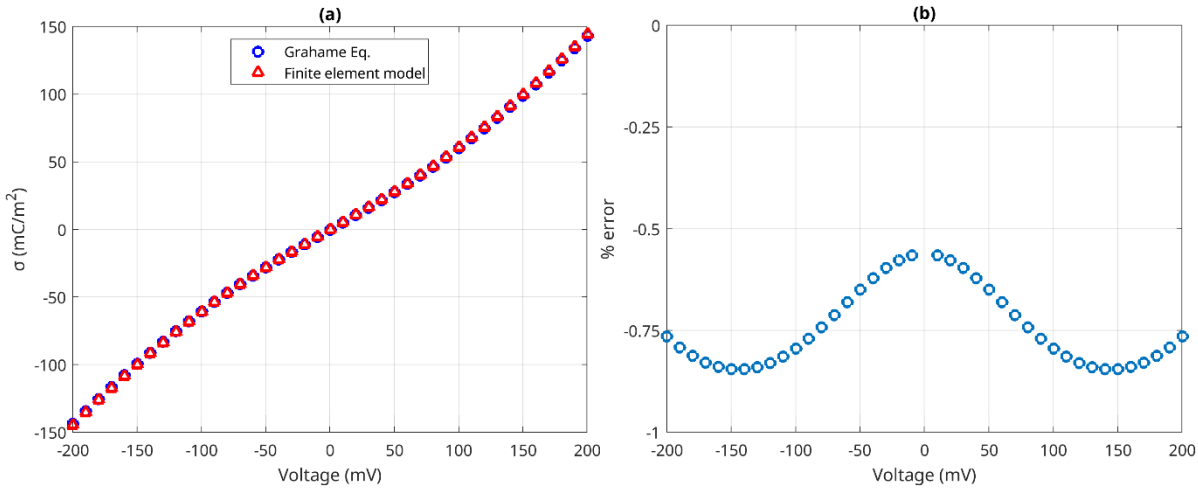

Figure S2.1 (a) The surface charge density, σ, on an ideally polarisable electrode was calculated for a range of input voltages using both the Grahame Eq. (S2.2) and by numerically integrating the concentration profiles from the finite element model described in the main text. (b) The percentage error shows that the two methods are in excellent agreement.

S3 Voltage-dependent ionic concentration profiles at the metal-electrolyte interface

Fig. S3.1 shows the spatial distribution of sodium (Na^+) and chloride (Cl^-) ion concentrations for negative voltages of −20 mV, −60 mV, and −200 mV, obtained using the coupled electrostatic and electrodiffusion model described in the main text. The x-axis represents the same spatial coordinate shown in Fig. 3a, moving away from the gold surface through the electric double layer. As expected, sodium ions accumulate near the metal surface under negative bias, while

chloride ions are depleted. This behaviour mirrors the trends observed under positive voltages, with opposite polarity. The concentration profiles confirm the exponential nature of ion accumulation and depletion with distance from the interface.

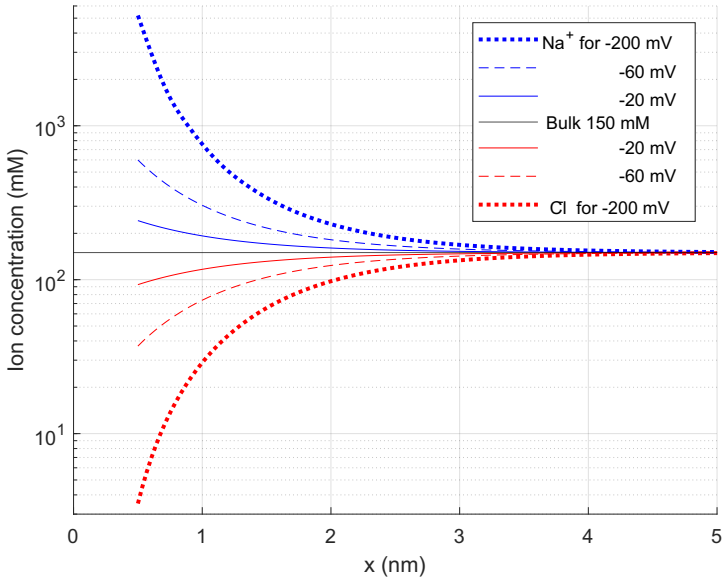

Figure S3.1 Spatial concentration profiles of Na^+ and Cl^- ions for applied voltages of −20 mV, −60 mV, and −200 mV. The ion distributions are plotted as a function of distance from the gold surface (x = 0), across the diffuse layer.

Fig. S3.2 presents the voltage-dependent ionic concentrations of Na^+ and Cl^- at the end of the Stern layer (0.5 nm from the metal surface). This data for negative voltages complements the selection of a ±200 mV range as the operational voltage window for the main study.

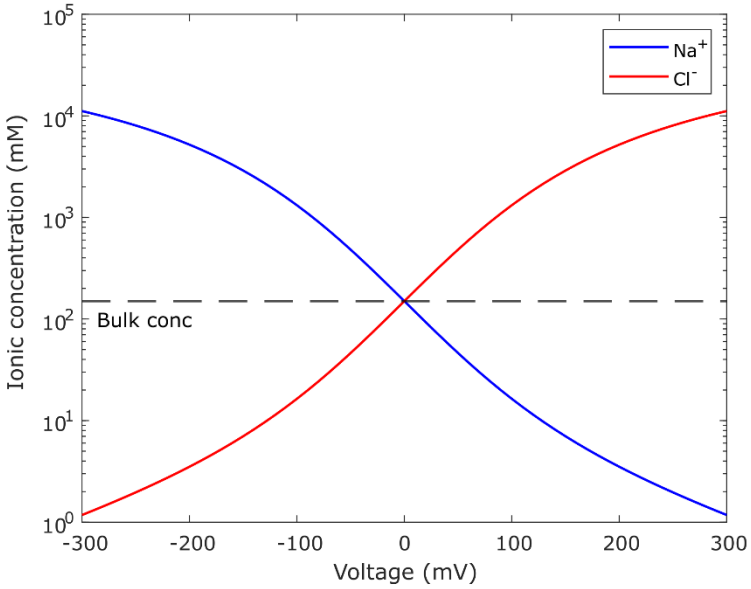

Figure S3.2 Voltage-dependent ionic concentrations of Na^+ and Cl^- at the end of the Stern layer.

S4 Extension to a charge-symmetric divalent electrolyte ($MgSO_4$)

The electrodiffusion modelling framework employed in the main text can be extended to charge-symmetric multivalent systems. To demonstrate this generalisation, we apply the same Stern–Poisson–Boltzmann formalism to a 2:2 magnesium sulfate ($MgSO_4$) electrolyte and compare the resulting ionic and optical responses to those obtained for NaCl under otherwise identical conditions.

In these simulations, $MgSO_4$ is treated as a fully dissociated symmetric divalent electrolyte, with bulk concentrations of Mg^{2+} and SO_4^{2-} each equal to 150 mM. All geometric parameters, dielectric properties, and electrostatic boundary conditions are kept identical to the NaCl case, such that differences between the two systems arise primarily from the increased ionic valence. In the COMSOL simulations, ion-specific transport properties were additionally updated to reflect the divalent electrolyte, with diffusion coefficients of $D_{Mg^{2+}} \approx 0.79 \times 10^{-9} m^2 s^{-1}$ and $D_{SO_4^{2-}} \approx 1.06 \times 10^{-9} m^2 s^{-1}$ [3]. The Stern layer thickness is assumed to be unchanged, while the diffuse layer is described using the nonlinear Poisson–Boltzmann equation for a symmetric Z:Z electrolyte with Z = 2.

Figure S4 compares the behaviour of $MgSO_4$ (coloured curves) with that of NaCl (grey curves). Panel (a) shows ion concentration profiles obtained from COMSOL simulations as a function of distance from the electrode for selected applied voltages. Compared to NaCl, the divalent electrolyte exhibits stronger counter-ion accumulation near the interface and a more rapid decay of concentration towards the bulk. This behaviour reflects the enhanced Boltzmann weighting associated with the higher ionic valence of the $MgSO_4$ solution, which reduces the effective Debye screening length.

Panel (b) presents the interfacial ion concentrations in the diffuse layer as a function of applied voltage, evaluated using the same fixed spatial analysis window as in the NaCl case. When averaged over this window, the interfacial concentrations for $MgSO_4$ and NaCl are found to be of comparable magnitude, despite the higher peak concentrations observed for $MgSO_4$ very close to the surface. This arises from the more rapid spatial decay of the divalent electrolyte concentration profile, such that the enhanced near-surface accumulation is confined to a narrower region.

The optical response for $MgSO_4$ is illustrated in panels (c) and (d). Panel (c) shows the refractive-index contributions associated with individual ionic species, demonstrating that the response is dominated by the counter-ion in both electrolytes, but with substantially larger magnitude for $MgSO_4$. This enhancement arises primarily from the larger molar refractivity of the sulfate ion compared to chloride, such that comparable concentration variations in the diffuse layer produce a stronger refractive-index modulation in the divalent electrolyte.

Panel (d) summarises the total refractive index change as a function of applied voltage. Despite the similar layer-averaged ion concentrations obtained for NaCl and $MgSO_4$ within the fixed analysis window, the larger molar refractivity of Mg and SO_4 ions leads to a significantly enhanced optical response, while preserving the same qualitative voltage dependence.

Taken together, these results confirm that the electrodiffusion framework used in the main text is applicable beyond monovalent electrolytes and that electrolyte-specific optical parameters play a central role in determining the magnitude of the voltage-induced refractive-index change.

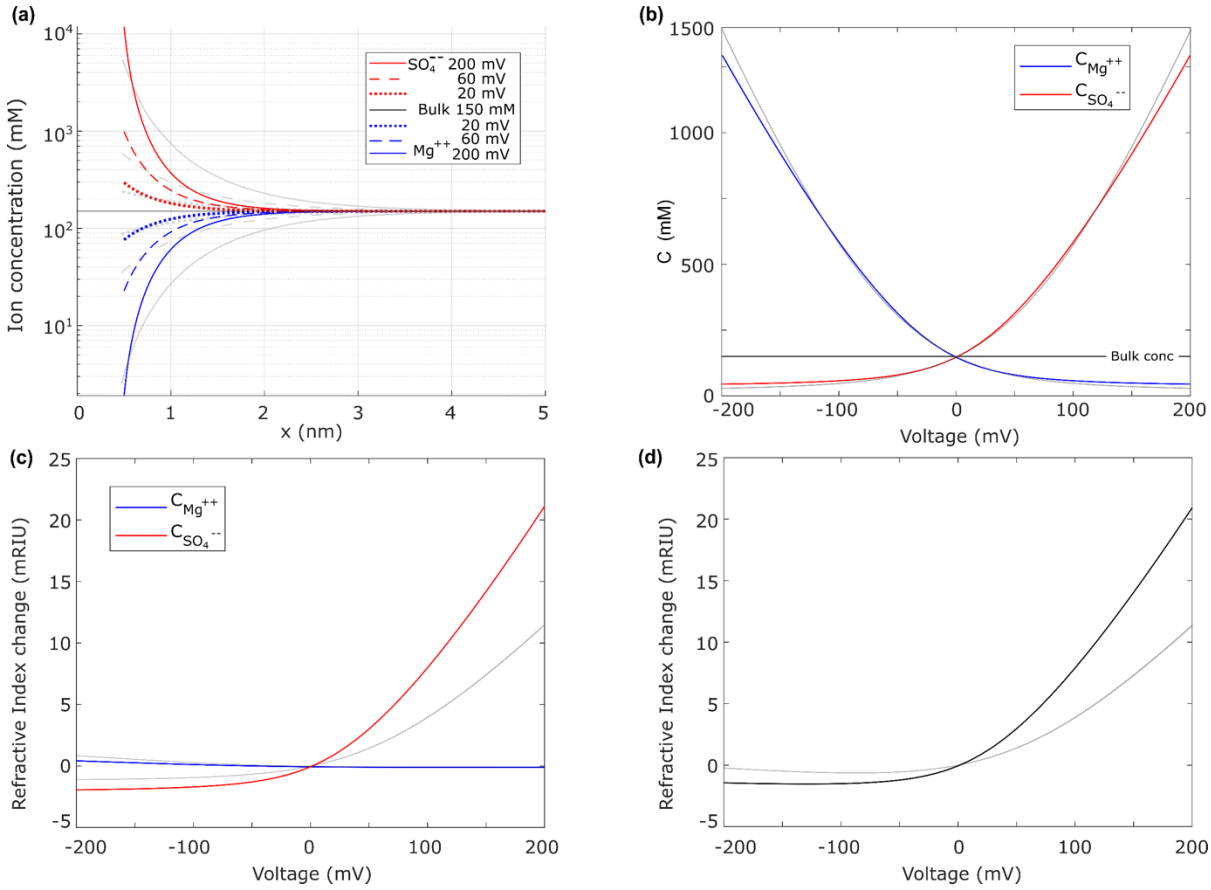

Figure S4. Comparison between NaCl and $MgSO_4$ electrolytes. (a) Ion concentration profiles as a function of distance from the electrode for selected applied voltages. (b) Interfacial ion concentrations versus applied voltage. (c) Refractive-index contributions from individual ionic species. (d) Total refractive-index change versus applied voltage. Grey, semi-transparent curves correspond to 0.15 M NaCl, while coloured curves correspond to 0.15 M $MgSO_4$.

<u>Molar refractivity parameters for $MgSO_4$</u>

The molar refractivity of magnesium sulfate was estimated from tabulated electronic ionic polarisabilities [4]. Electronic ionic polarisabilities for Mg^{2+} and SO_4^{2-} were taken from the work of Tessman, Kahn, and Shockley, who derived effective ionic values from the optical properties of ionic crystals.

For Mg^{2+}, an electronic polarisability of $\alpha_{Mg^{2+}} = 0.094 \mathring{A}^3$ was adopted. For the sulfate anion, Tessman *et al.* reported an effective electronic polarisability in the range $\alpha_{SO_4^{2-}} = 3.0 - 5.3 \mathring{A}^3$.

In the present work, a representative midpoint value of $\alpha_{SO_4^{2-}} \approx 4.1 \mathring{A}^3$ was used, with the reported range taken as an estimate of uncertainty associated with variations in the ionic environment.

The corresponding molar refractivities were obtained using the Lorentz–Lorenz relation,

$$R = \frac{4\pi N_A}{3}\,\alpha, \qquad \text{(S4.1)}$$

yielding $R_{Mg^{2+}} \approx 0.237\ \text{cm}^3\ \text{mol}^{-1}$, $R_{SO_4^{2-}} \approx 10.340\ \text{cm}^3\ \text{mol}^{-1}$.

S5 - Transmission *line model of multilayer sensing structures*

This method focuses on wave impedance in uniform, non-magnetic media with permittivity $\varepsilon = \varepsilon_0 \varepsilon_r$.

The wave impedance Z_0 is defined as the ratio of electric (E_0) and magnetic (H_0) fields' complex amplitudes:

$$Z_0 = \frac{E_0}{H_0} = \sqrt{\frac{\mu_0}{\varepsilon_0 \varepsilon_r}} \quad \text{(S5.1)}$$

This is particularly useful for analysing transverse electric (TE) and transverse magnetic (TM) waves at oblique angles θ, where wave impedance in non-magnetic material is:

$$Z_{TM} = \sqrt{\frac{\mu_0}{\varepsilon_0}}\frac{cos\,\theta}{n}\ ; \quad Z_{TE} = \sqrt{\frac{\mu_0}{\varepsilon_0}}\frac{1}{n\,cos\,\theta} \quad \text{(S5.2)}$$

The standard formula for the reflection coefficient, ρ, in terms of wave impedance is

$$\rho = \frac{\mathrm{Z}_{in} - Z_G}{\mathrm{Z}_{in} + Z_G} \quad \text{(S5.3)}$$

where Z_G is the wave impedance of the incident medium (the generator) and Z_{in} is the input impedance or effective impedance seen at the generator interface.

The calculation of Z_{in} involves propagating the wave impedance through each layer of the multilayer system, starting from the last layer (at the load side, rightmost) and progressing toward the generator interface, as shown in Fig. S5. This is achieved using the recursive impedance relation:

$$Z_{in,i} = Z_i \left[\frac{Z_{in,i+1} + Z_i \tanh\left(ik_{z,i}d_i\right)}{Z_i + Z_{in,i+1} \tanh\left(ik_{z,i}d_i\right)}\right]. \quad \text{(S5.4)}$$

Here, Z_i is the characteristic wave impedance, $k_{z,i}$ is the z-component of the propagation constant and d_i the thickness of the i-th layer. This iterative approach ensures efficient calculation of the reflectivity for the entire multilayer structure [5].

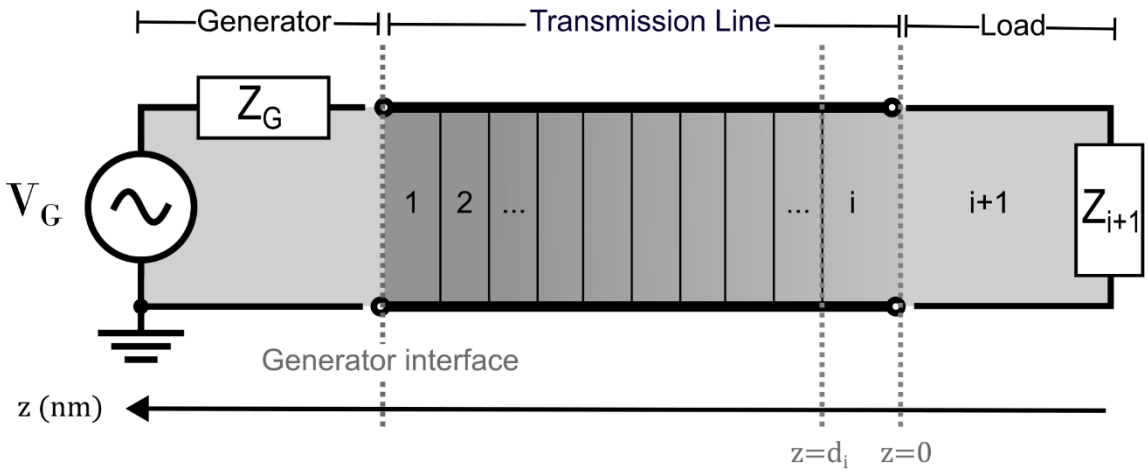

Figure S5. Transmission line model for multilayer sensing structures. The system consists of a generator with voltage V_G and impedance Z_G, connected to a stratified medium composed of multiple layers with varying permittivity $\varepsilon = \varepsilon_0\varepsilon_r$. Each layer contributes to the overall input impedance Z_{in} seen at the generator interface, calculated recursively from the load Z_{i+1} back toward the source.

S6 – Mie modelling of scattering by gold nanoparticles

This section details the numerical implementation of the Mie scattering model used to simulate the optical response of voltage-modulated plasmonic nanoparticles. The model is based on Peña and Pal's analytical extension of Mie theory to multilayered spheres, implemented using the *scattnlay* function [6]. Each layer in the nanoparticle–electrolyte system is characterised by its refractive index and thickness as described in the main Methods section. To compute the scattering properties, each layer is assigned a size parameter

$$x_l = \frac{2\pi N_m r_l}{\lambda} \quad \text{(S6. 1)}$$

and a relative refractive index

$$m_l = {N_l}/{N_m} \quad \text{(S6. 2)}$$

where r_l is the outer radius of layer l, N_l is its refractive index, N_m is the surrounding medium's index, and λ is the vacuum wavelength.

To calculate the scattering of a multilayered sphere, the electromagnetic fields in each layer are expressed in terms of spherical wave functions. The total fields inside and outside the particle are represented as superpositions of spherical eigenfunctions that satisfy Maxwell's equations, with continuity conditions applied at each interface. The Mie scattering coefficients a_n and b_n are obtained by solving boundary conditions for each multipole order n, using recursive formulations involving Riccati–Bessel functions, as described by Yang [7] and Kerker [8]. These coefficients are then used to compute the extinction, scattering, and absorption efficiencies (Q_{ext}, Q_{sca} and Q_{abs}):

$$Q_{ext} = \frac{2}{x_L^2}\sum_{n=1}^{\infty}(2n+1)Re\{a_n + b_n\} \qquad \text{(S6. 3)}$$

$$Q_{sca} = \frac{2}{x_L^2}\sum_{n=1}^{\infty}(2n+1)(|a_n|^2 + |b_n|^2) \qquad \text{(S6. 4)}$$

$$Q_{abs} = Q_{ext} - Q_{sca} \qquad \text{(S6. 5)}$$

These efficiencies are converted to physical cross-sections using $C = AQ$, where $A = \pi r_L^2$ is the geometric cross-section. The subscript r_L refers to the outermost radius of the multilayered particle.

To identify the unperturbed resonance wavelength, a coarse spectral scan was performed over the 400–800 nm range in 1 nm steps. Once the resonance peak was located, a refined spectral scan was carried out over a ±50 nm window centred around the peak, using 1 Å steps, for applied voltages ranging from –200 mV to +200 mV in 1 mV increments. Scattering calculations were performed assuming illumination by a linearly polarised plane wave. The nanoparticle was treated as free-floating in a homogeneous electrolyte, i.e., no substrate was included.

This model includes the following assumptions. Nanoparticles are assumed to be spherical and suspended in bulk solution, without accounting for interactions with a substrate. The incident illumination is modelled as a linearly polarised plane wave, which is a suitable approximation for optically symmetric particle geometries. Finally, the diffuse layer was discretised into two sublayers, which is sufficient to capture the main features of the exponential potential decay while keeping the optical model

tractable. Although additional sublayers could provide finer spatial resolution, tests showed that they do not significantly alter the calculated optical response, so two layers were adopted for efficiency.

References

1. A. J. Bard and L. R. Faulkner, *Electrochemical Methods: Fundamentals and Applications*, John Wiley & Sons, New York, NY, 2nd edn, 2001.
2. J. N. Israelachvili, *Intermolecular and Surface Forces*, Academic Press, Amsterdam, 3rd edn, 2011, ch. 14, pp. 291–340.
3. *CRC Handbook of Chemistry and Physics*, ed. W. M. Haynes, CRC Press, Boca Raton, FL, 97th edn, 2016.
4. J. R. Tessman, A. H. Kahn and W. Shockley, *Phys. Rev.*, 1953, **92**, 890–895.
5. M. G. Somekh, K. Regules-Medel and S. A. Abayzeed, *J. Opt. Soc. Am. A*, 2024, **41**, C90–C98.
6. O. Peña and U. Pal, *Comput. Phys. Commun.*, 2009, **180**, 2348–2354.
7. W. Yang, *Appl. Opt.*, 2003, **42**, 1710–1720.
8. M. Kerker, *The Scattering of Light and Other Electromagnetic Radiation*, Academic Press, New York, 1969, vol. 16.